Check for updates

Cell response and bone ingrowth to 3D printed Ti6Al4V scaffolds with Mg-incorporating sol–gel Ta_2O_5 coating†

Bo Zhang,‡[a] Jun Feng,‡[a] Shuo Chen,[a] Ruohan Liao,[a] Chengdong Zhang,[ab] Xuwei Luo,[a] Zelong Yang,[a] Dongqin Xiao, ⓘD *[a] Kui He[c] and Ke Duan*[c]

In recent years, additive manufacturing techniques have been used to fabricate 3D titanium (Ti)-based scaffolds for production of desirable complex shapes. However, insufficient osteointegration of porous Ti-based scaffolds can elicit long-term complications (e.g., aseptic loosening) and need further revision surgery. In this study, a magnesium (Mg)-incorporating tantalum (Ta) coating was deposited on a 3D Ti6Al4V scaffold using a sol–gel method for enhancing its osteogenic properties. To evaluate the biofunction of this surface, bone mesenchymal stem cells and rabbit femoral condyle were used to assess the cell response and bone ingrowth, respectively. Ta_2O_5 coatings and Mg-incorporating Ta_2O_5 coatings were both homogeneously deposited on porous scaffolds. In vitro studies revealed that both coatings exhibit enhanced cell proliferation, ALP activity, osteogenic gene expression and mineralization compared with the uncoated Ti6Al4V scaffold. Especially for Mg-incorporating Ta_2O_5 coatings, great improvements were observed. In vivo studies, including radiographic examination, fluorochrome labeling and histological evaluation also followed similar trends. Also, bone ingrowth to scaffolds with Mg-incorporating Ta_2O_5 coatings exhibited the most significant increase compared with uncoated and Ta_2O_5 coated scaffolds. All the above results indicate that Mg-doped Ta_2O_5 coatings are an effective tool for facilitating osteointegration of conventional porous Ti6Al4V scaffolds.

Introduction

Additive manufacturing, also known as 3D-printing, has become a unique technique for producing orthopaedic devices because of its ability to manufacture prostheses of customized geometries and well controlled porous structures.[1,2] In orthopaedics, these advantages can readily translate to designable mechanical properties (e.g., stress distribution) and improved bone ingrowth (i.e., biological fixation). As a result, 3D-printed porous titanium (Ti) implants are increasingly used for the repair of complex bone defects.

Nevertheless, Ti is considered a relatively bioinert metal, as it does not form chemical bonding to bone tissue.[3,4] Moreover, although porous Ti implants accommodate bony ingrowth to achieve biological fixation, there has been a persistent desire to accelerate this process, thereby allowing early mobility and functional exercise for the patient. Consequently, improving the surface bioactivity of porous Ti implants is an important endeavor toward accelerating their biological fixation.

In the past two decades, tantalum (Ta) has emerged as a successful orthopaedic metal. Porous Ta with trabecular-bone-like microstructures has been validated to elicit extensive ingrowth in animals and humans,[5,6] and is now widely used in orthopaedics in various forms such as structural grafts, acetabular cups, and surface coatings.[7–9] Lu et al. compared in vivo bone ongrowth to Ti and Ta by placing cylindrical samples in distal femurs of ovariectomized rats; they found that, 8 weeks after implantation, Ta had a significantly longer bone-implant contact percentage than Ti.[10] Additionally, several studies reported that, Ta increased (vs. Ti) the osteogenic activities of animals or cells under conditions related to compromised bone formation (i.e., osteoporosis, diabetes, advanced age),[11,12] suggesting that Ta implants may gave improved outcomes for patients with these conditions. The favorable properties of Ta result, at least partly, from its excellent corrosion resistance and biocompatibility, properties primarily attributed to the native

[a]Research Institute of Tissue Engineering and Stem Cells, Department of Orthopaedics, Nanchong Central Hospital, The Second Clinical College of North Sichuan Medical College, Nanchong, Sichuan 637000, China. E-mail: xiaodongqin@nsmc.edu.cn; keduan@swmu.edu.cn

[b]Key Laboratory of Advanced Technologies of Materials (MOE), School of Materials Science and Engineering, Southwest Jiaotong University, Chengdu, Sichuan 610031, China

[c]Sichuan Provincial Laboratory of Orthopaedic Engineering, Department of Orthopaedics, Affiliated Hospital of Southwest Medical University, Luzhou, Sichuan 646000, China

passivation film (Ta_2O_5) that forms spontaneously on the surface of Ta. However, compared with Ti, Ta also exhibits major disadvantages such as a lower tensile strength (138–470 *vs.* 380–860 MPa) and higher density (16.6 *vs.* 4.4 g cm^{-3}), cost (~10 fold higher than Ti), and modulus (~190 *vs.* ~110 GPa). Considering their comparative strengths and limitations, it follows that depositing Ta or Ta_2O_5 as a surface coating on Ti may be a reasonable design combining the advantages of the two materials.

Earlier studies have reported several techniques of depositing Ta or Ta_2O_5 coatings on Ti. Balla *et al.* prepared a Ta coating on Ti by laser cladding, and reported improved (*vs.* uncoated Ti) adherence and growth of human osteoblasts.[13] Wang *et al.* deposited a metallic Ta coating on 3D-printed porous Ti scaffolds by chemical vapor deposition (CVD), and observed attenuated reactive oxygen species generation and improved osteoblastic cell interactions in a simulated *in vitro* diabetic environment.[11] Lin *et al.* prepared Ta_2O_5 coatings on Ti6Al4V by plasma spray, and found the coating to enhance the attachment, spreading, and proliferation of osteoblast-like cells.[14] However, plasma spray and laser cladding are line-of-sight techniques that are difficult to apply on parts of complex geometries (*e.g.*, porous Ti). CVD, on the other hand, requires highly special facilities (*i.e.*, CVD reactor), which may limit the application of the technique.

To optimize the bioactivity of metallic implants, various strategies have been used to impart desirable functions such as osteoinductivity and antibacterial actions. Of these, incorporation of trace metallic ions has gained intensive interests partly because of their lower costs and greater stability against denaturing and sterilization (*vs.* biological factors). Magnesium (Mg) is an essential element that directly participates in the bone calcification process and the production of new minerals in human bodies. At appropriate concentrations/doses, Mg^{2+} addition was reported to promote osteogenic differentiation of stem cells, enhance the angiogenesis of vascular endothelial cells as well as accelerate the osseointegration of implants *in vivo*.[15,16] Also, Mg ions could suppress the release of inflammatory cytokines and induce macrophages towards M2 phenotype.[17] An additional major advantage of Mg is its relative abundance in the human body (~20–30 g g per adult) and, thus, comparative safety. Gao *et al.* deposited Mg coating on porous Ti6Al4V by ion sputtering and reported the coating to improve the *in vitro* response (adhesion, proliferation, osteoblastic differentiation) of MC3T3-E1 cells and new bone formation in a rabbit model.[18]

To combining the advantages of Ta and Mg with Ti, we previously developed a simple sol–gel technique for coating T_2O_5 and Mg-doped T_2O_5 on Ti, and found positive *in vitro* effects from coated flat Ti samples.[19] In the present study, we applied Mg-doped T_2O_5 onto 3D-printed porous Ti scaffolds and evaluated their capacities *in vitro* and *in vitro* response.

Materials and methods

Materials preparation

Porous scaffolds were printed with Ti6Al4V powders (particle size: 15–53 μm, AMC Powders Metallurgy Technology, Beijing, China) by selective laser melting (FS271M 3D Printer, Huashu Turin Additive Manufacturing Technology, Chengdu, Sichuan, China) as reported previously.[20] The scaffolds had a simple cubic lattice structure, with a pore size of ~600 μm and strut size of ~250 μm, thus giving a porosity of ~70%. Scaffolds with a size of 12 × 12 × 2 mm were used for cell culture, and those with size of 4 × 4 × 8 mm was used for animal implantation (ESI Fig. S1†). After printing, all samples were cleaned by sonicating sequentially in acetone, ethanol, and water.

Mg-doped Ta_2O_5 were coated on the scaffolds by a sol–gel method.[19] Briefly, 0.5 ml of tantalum ethoxide (Sigma), 0.64 ml of diethanolamine, and 0.62 ml of water were successively added into in ethanol, respectively. Magnesium acetate (Aldrich) was dissolved into the aforementioned tantalum oxide/ethanol solution at a Mg/Ta molar ratio of 0.25. After stirring for 30 min, the solution was left to stand at room temperature for 24 h to form a yellowish sol. Subsequently, the porous scaffold was immersed into the sol, and kept for 5 s, and vertically withdrawn at 1 mm s^{-1}. Then, the scaffold was dried in air, and the dip-coating procedure was repeated once. After drying in air, the scaffold was calcinated at 600 °C in a muffle furnace for 2 h. For preparation of pure (Mg-free) Ta_2O_5 coating, magnesium acetate was omitted and all other procedures were identical. In following sections, the pristine scaffold was abbreviated as PTi; the one coated with Ta_2O_5 as PTi-Ta, and the one coated with Mg-doped Ta_2O_5 as PTi-Ta–Mg. Unless otherwise stated, all reagents were analytical grade and from Kelong Chemical (Chengdu, Sichuan, China).

Characterizations

Microstructure and chemical composition were characterized with a scanning electron microscope (SEM, FEI Quanta200) and the equipped energy dispersive spectrometer (EDS), respectively. To measure concentrations of Ca^{2+} and Mg^{2+}, scaffolds were immersed into phosphate buffer saline (PBS) without Ca^{2+} and Mg^{2+}. After 1, 7, 14 and 24 days, the supernatant was collected and analyzed by inductively coupled plasma mass spectrometry (ICP-MS, NexION 1000, USA).

In vitro cytocompatibility

Bone marrow-derived mesenchymal stem cells (BMSCs) isolated[21] from a New Zealand white rabbit were cultured in Dulbecco's modified eagle's medium (DMEM) supplemented with 10% fetal bovine serum and 1% penicillin-streptomycin and passaged. PTi, PTi-Ta, and PTi-Ta–Mg were sterilized by autoclaving (121 °C, 30 min) and placed into culture wells. BMSCs at passage 2 were seeded on the scaffolds (4 × 10^4 cells per well) and cultured (37 °C, 5% CO_2) with one medium renewal every 2 days.

After culture for 72 h, the scaffolds were removed, rinsed with PBS, and fixed in 4% paraformaldehyde for 30 min. After rinsing with PBS, some scaffolds were stained using 4′, 6-diamidino-2-phenylindole (DAPI, Beyotime, China) and iFluor488-labeled phalloidin (Beyotime, China). Then, the cell morphology was observed by laser scanning confocal microscopy (Olympus FV3000). The other scaffolds were live/dead

stained with 2 μmol l^{-1} calcein-AM and 4 μmol l^{-1} propidium iodide (PI), and observed by fluorescence microscopy (Leica DMi8). Additionally, after culture for 1, 4, and 7 days, cell proliferation was determined with cell counting kits (CCK-8, Vazyme, China).

In vitro osteogenic induction

Moreover, after culture as described in section 2.3 for 4 days, the culture medium was replaced with an osteogenic induction medium (DMEM with 10% fetal bovine serum, and 10 nM dexamethasone, 10 mM β-glycerophosphate and 50 μg ml^{-1} ascorbic acid). Then, after culture of 7 and 14 days, alkaline phosphatase (ALP) levels were measured from some samples using ALP microplate kits (Beyotime, China). Meanwhile, the expression of several osteogenesis-related genes [*i.e.*, ALP, runt-related transcription factor 2 (Runx2), osteopontin (OPN), and ostocalcin (OCN) were measured by quantitative real-time polymerase chain reaction (Q-PCR) using a PCR machine (Bio-Rad T100) and SYBR Green Q-PCR kits (Vazyme, China). The primers are listed in ESI Table S1.† Expression levels were determined by the $2^{-\Delta\Delta CT}$ method and normalized to the housekeeping gene (β-actin). After culture for 21 days, the scaffolds were fixed using paraformaldehyde (4%) and stained using alizarin red S solution (1%) (Beyotime, China). After repeated rinses with water, the scaffolds were observed under a stereomicroscope for the presence of mineralized nodules.

In vivo implantation model

All animal procedures were performed in accordance with the Guidelines for Care and Use of Laboratory Animals of the National Institutes of Health and approved by the Animal Ethics Committee of North Sichuan Medical College. Forty-five New Zealand white rabbits (age: 3 months, weight: ~2.5 kg; Center of Laboratory Animals of North Sichuan Medical College) were used. The animals were randomized into 3 groups to receive implantation of PTi, PTi-Ta, or PTi-Ta–Mg ($n = 15$/group). After anesthesia by intravenous injection of 2% pentobarbital sodium (2 ml kg^{-1}), a longitudinal incision (1.5 cm) was made on the skin over the lateral femoral condyle; the incision was blunt separated; and a hole (ϕ 4 × 8 mm) was slowly drilled into the center of the femoral condyle, all under continuous saline irrigation. The scaffold was implanted into the hole (ESI Fig. S2†).[22] The wound was closed in layers with sutures and disinfected with povidone-iodine. After operation, all rabbits received intravenous penicillin (6000 IU/kg) for 3 days and regularly monitored for diet intake and physical activities. To label the fronts of osteogenesis, three fluorescent bone markers (calcein, Sigma, 5 mg ml^{-1}; xylenol orange, Sigma, 50 mg ml^{-1}; tetracycline, Sigma, 10 mg ml^{-1}) were intravenously injected into rabbits at specific times, respectively. In brief, for animal sacrificed at 4 weeks, calcein, xylenol orange and tetracycline were intravenously injected at 1, 2, 3 weeks after operation, respectively. For animal sacrificed at 8 weeks, these markers were injected at 2, 4, 6 weeks, respectively. For animal sacrificed at 12 weeks, the injections were carried out at 3, 6, 9 weeks, respectively.

At 4, 8, and 12 weeks after implantation, five animals per group were sacrificed by pentobarbital overdosing. Femoral condyle specimens were collected and fixed in 10% formalin. After gross observation, X-ray examination, microscopic computed tomography (CT) scanning (micro-CT, Scanco, uCT100), specimens were dehydrated in graded series of ethanol (70–100%), mounted in poly(methylmethacrylate) (PMMA, Aorigin, China), and sectioned parallel to the longitudinal axis of the scaffold using a diamond saw (~10 μm; SAT-001 Aorigin, China). The sections were stained with 1% methylene blue and 0.3% basic fuchsine (Aldrich) and observed with an inverted phase-contrast light microscope (Leica DMi8) for histological analysis. Additionally, the slices stained with calcein green, xylenol orange, and tetracycline were observed with a laser scanning confocal microscope (LSCM, Nikon A1). Photomicrographs were quantified with Image J software.

Statistical analysis

Data were analyzed by analysis of variance (ANOVA) and Tukey multiple comparison tests (SPSS 19.0, IBM, Armonk, NY, USA). A $p < 0.05$ was considered statistically significant.

Results

Scaffold characteristics

SEM showed that, the three groups of scaffolds (Fig. 1A) had similar microstructures characterized by square cells (side length: ~600 μm) and struts (thickness: ~250 μm). At higher magnifications (Fig. 1B), spherical Ti powder particles were observed to attach to the edge of PTi struts. In comparison, the struts of PTi-Ta and PTi-Ta–Mg (Fig. 1B) were covered with a relative smooth coating and no protruding Ti particles were directly seen. EDS detected Ti, Al, and V from PTi (Fig. 1C). As expected, Ta was additionally detected from PTi-Ta, and Ta and Mg from PTi-Ta–Mg. In our previous study,[19] X-ray diffraction
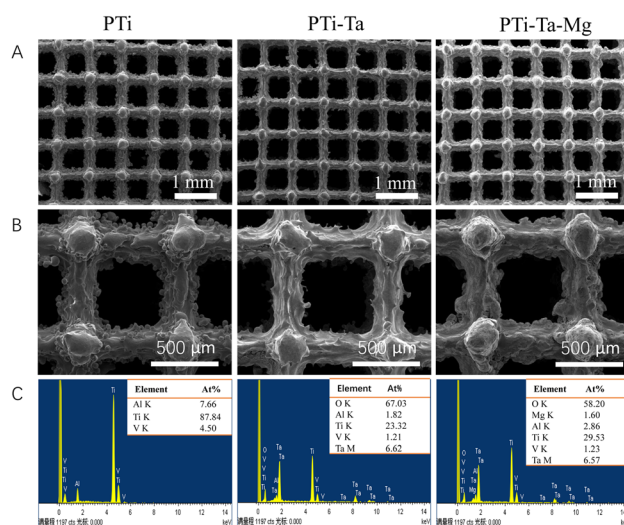

Fig. 1 (A and B) Scanning electron micrographs and (C) energy dispersive X-ray spectra of different 3D-printed scaffolds.

found peaks of crystalline Ta_2O_5 from a powder prepared by the sol–gel method, whereas only highly diffused peaks were detected at 20–40° and 40–60° from PTi-Ta–Mg. These results indicate that crystalline Ta_2O_5 was deposited on PTi-Ta whereas an amorphous oxide was coated on PTi-Ta–Mg. In addition, the depositions of Ta_2O_5 and Mg-incorporating Ta_2O_5 coatings did not significantly affect the surface roughness of Ti surface. However, the both coatings could decrease the water contact angle of Ti surface from ∼62° to 21°∼23°, indicating the enhanced hydrophilicity.[19]

Ion release

The cumulative release curve (ESI Fig. S3†) showed that the sample PTi-Ta–Mg demonstrated a sustained release of Mg ions. After immersion in PBS for 24 days, the cumulative release reached ∼4.8 μg. In comparison, relative low amounts of Ta ions were detected for both PTi-Ta–Mg and PTi-Ta. The Mg ions release amount was ∼1600 times higher than that of Ta ions after 24 days.

Cellular response including adhesion, proliferation and ALP activity

Live/dead staining (Fig. 2A) revealed that, after culture for 72 h, viable rBMSCs were prevalent on all scaffolds and followed the rank: PTi-Ta–Mg > PTi-Ta > PTi. Moreover, the cells adhered and flattened on the scaffolds (Fig. 2B). Compared with cells on PTi, those on PTi-Ta emitted a stronger fluorescence and more F-actin fibers, while those on PTi-Ta–Mg exhibited the highest density of F-actin fibers. CCK-8 assays (Fig. 2C) indicated that, the cells proliferated on all scaffolds with the elapse of time in

culture. On day 4, the cell numbers measured from PTi-Ta and PTi-Ta–Mg were significantly higher than that from PTi (both p < 0.03). On day 7, the cell number followed the rank: PTi-Ta–Mg > PTi-Ta > PTi, and the difference between each group pair was statistically significant (all p < 0.02).

After culture in osteogenic induction medium for 7 days, all groups had similar ALP levels, and no significant difference was found among the three groups (ANOVA). On day 14, ALP activities in PTi-Ta and PTi-Ta–MgP became significantly higher than that in PTi (both p < 0.001). Moreover, the ALP activity in PTi-Ta–Mg was also significantly higher than that in PTi-Ta (p = 0.01).

Bone-related gene expression and *in vitro* mineralization

PCR found that, after culture in osteogenic induction medium for 7 days (Fig. 3A), the ALP gene expression levels in PTi-Ta and PTi-Ta–Mg groups were significantly higher than that in PTi (both p < 0.05). And, the Runx2 gene expression level in PTi-Ta group was significantly higher than that in PTi group. However, no significant difference was observed in OPN and OCN expressions among the three groups. On day 14, the expressions levels of ALP, OPN, OCN and Runx2 genes all followed the trend: PTi-Ta–Mg > PTi-Ta > PTi (Fig. 3B). More quantitatively, compared with PTi, the ALP gene expression levels in PTi-Ta and PTi-Ta–Mg were increased by 28% (p = 0.0048) and 54% (p = 0.0014), respectively. Moreover, for OPN, the counterpart increases were 51% (p = 0.0024) and 73% (p = 0.0003), respectively. For Runx2, the increases were 46% (p = 0.04) and 70% (p = 0.0096). For OCN, the gene expression level in PTi-Ta–Mg were 88% higher than that on PTi-Ta (p = 0.0038) and 120% higher than that on PTi (p = 0.0017), respectively. These increases were all statistically significant.

Alizarin red staining (Fig. 3B) found that, after culture in osteogenic induction medium for 21 days, red mineralized nodules (stained as red patches) were observed on all scaffolds. The largest red areas were observed on PTi-Ta–Mg followed by PTi-Ta and then PTi.
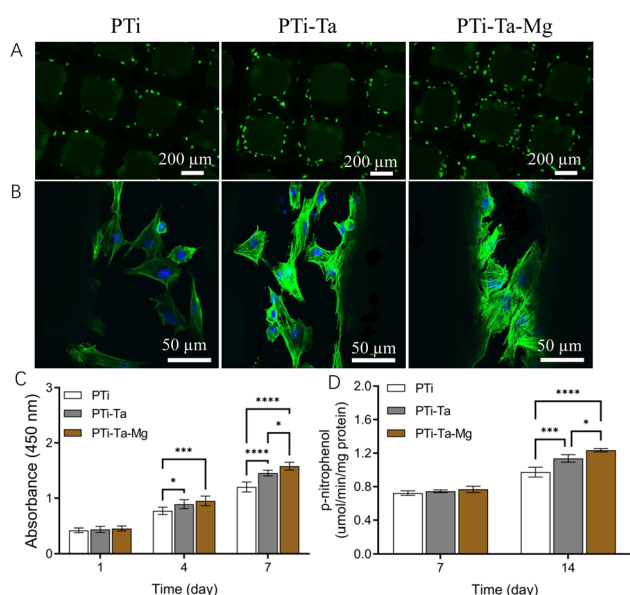

Fig. 2 (A) Live/dead cells staining of rBMSCs cultured on different scaffolds for 72 h; (B) cytoskeletal F-actin (green) and nuclei (blue) staining of the cells cultured on different scaffolds for 72 h; (C) cell proliferation on different samples for 1–7 days; (D) ALP activities of the cells cultured on different samples for 7 and 14 days; *: p < 0.05; ***: p < 0.001; ****: p < 0.0001.
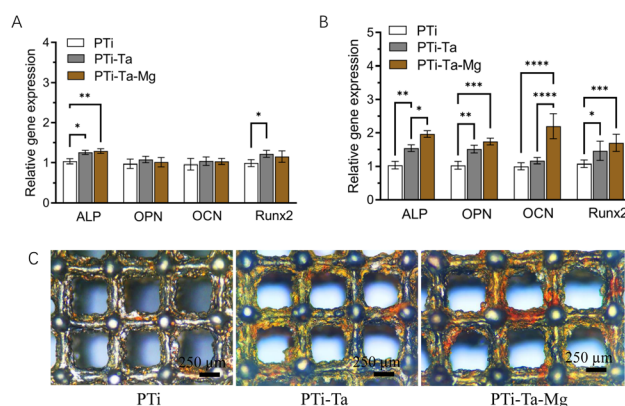

Fig. 3 Expression levels of bone-related genes measured by PCR from rBMSCs cultured on different scaffolds for (A) 7 days and (B) 14 days (*: p < 0.05; **: p < 0.01; ***: p < 0.001; ****: p < 0.0001); (C) photomicrographs showing *in vitro* formation of mineralized nodule (red patches) by the cells cultured on different scaffolds in osteogenic induction medium for 21 days.

In vivo bone formation

Gross examination and X-ray radiograph. Four, eight, and twelve weeks after implantation, the femoral condyles were harvested and visually examined (ESI Fig. S4†). At week 4, all scaffolds were found to be well positioned in place, without visible signs of inflammatory reaction or displacement. The pores on scaffold surface were clearly visible from all groups. At week 12, more new tissue encapsulated and infiltrated all scaffolds. This was especially evident for PTi-Ta and PTi-Ta–Mg, whereas the PTi scaffold was still partly visible (un-encapsulated).

X-ray radiography confirmed that all scaffolds were perfectly matched the femoral condyle without any displacement (Fig. 4). At week 4, the edges and pores of all implants were all visible, especially clear for PTi. At week 8, the X-ray absorption by all scaffolds increased noticeably (*vs.* week 4). For PTi, the edges of the implants became blurred, while the pores were still clear. In comparison, for PTi-Ta and PTi-Ta–Mg, their edges and pores appeared blurred, indicating higher overall densities than that of PTi. At week 12, the X-ray absorption by all scaffolds further increased, exhibiting further blurring of implant edge and pores, indicating continued new tissue ingrowth/infiltration. In particular, for PTi-Ta–Mg, it became difficult to discern the pores, indicating the most bone ingrowth.

Micro-CT imaging. Fig. 5A shows representative reconstructed micro-CT images. At week 4, all groups showed similar bone ingrowth. PTi-Ta and PTi-Ta–Mg seemed to had more bone attachment to struts, particularly at the central region, but the difference was subtle. At week 12 (Fig. 5A), clearly, more extensively bone ingrowth into the central region was seen in PTi-Ta and PTi-Ta–Mg than in PTi, especially in the center of PTi-Ta–Mg. Quantitatively, all groups displayed a trend of continued bone formation with time (Fig. 5B). At each time point, the BV/TV (new bone volume/total volume) ratio followed the trend: PTi < PTi-Ta < PTi-Ta–Mg, and the differences between all group pairs were statistically significant (all p < 0.02).

Fluorescent bone labelling. To reveal *in vivo* bone formation, three fluorescent dyes [calcein (green fluorescence), xylenol orange (red fluorescence) and tetracycline (yellow fluorescence)] were injected in animal. The amount of newly formed bone was
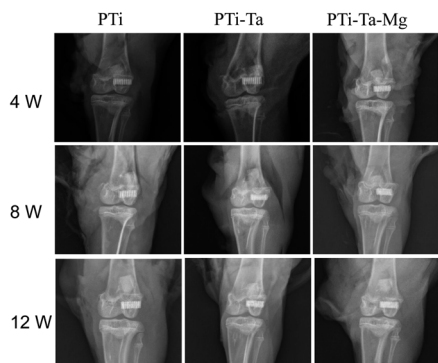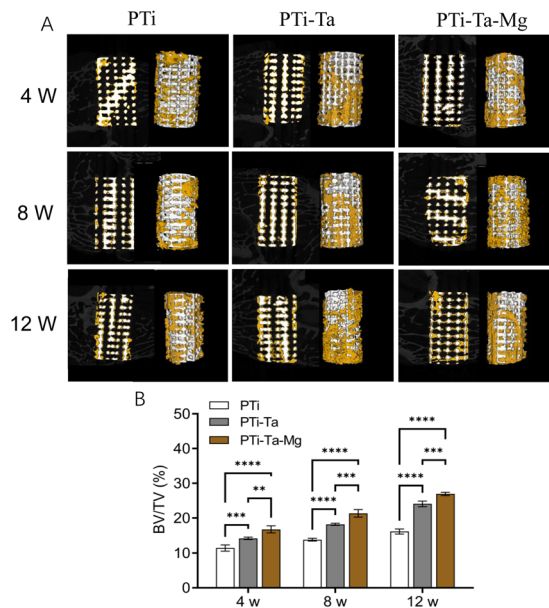

Fig. 5 (A) 3D reconstructed micro-CT images of different scaffolds implanted in the femoral condyles *in vivo* after 4, 8 and 12 weeks. The yellow color indicates the bone formation in the porous scaffolds, while the light gray color indicates the scaffold. (B) Quantitative analysis of new bone formation in the scaffolds evaluated using BV/TV (bone volume/total volume). **: p < 0.01; ***: p < 0.001; ****: p < 0.0001.

quantified using the percentage of bone area/total area. Overlaid fluorescent images showed that, at week 4 (Fig. 6A), in all groups new bone formed in the region peripheral to the scaffold, without noticeable bone formation in the central space. Quantitative analysis found new bone percentages (bone volume/total volume) in scaffolds followed the trend: PTi-Ta–Mg > PTi-Ta > PTi. And, the differences were all statistically significant (all p < 0.05).

At week 8, new bone area, as represented by fluorescence pixels, increased (*vs.* week 4) in all groups. PTi showed sporadic new bone (yellow fluorescence) distributed in the central space. For PTi-Ta, evident yellow and red fluorescences were seen in the central space. For PTi-Ta–Mg, diffused (nearly continuous) fluorescence was emitted from the peripheral as well as the central regions. The percentage of new bone in PTi was 36% lower than in PTi-Ta and 57% lower than in PTi-Ta–Mg. Also, the differences between PTi and the other two groups were both statistically significant (both p < 0.0001).

At week 12, new bone area further increased (*vs.* week 8) in all groups; new bone was not only in the peripheral region but also in the central space. The percentage of new bone in PTi was 25% lower than in PTi-Ta and 43% lower than in PTi-Ta–Mg. Again, the differences between PTi and other two were both statistically significant (both p < 0.0001).

Histological evaluation. Methylene blue-basic fuchsin staining (Fig. 7) revealed that, at week 4, in all groups new bone formed predominantly in the peripheral region. Negligible new bone was also observed in the internal space of PTi-Ta and, in particular, PTi-Ta–Mg. At week 8, in all groups, more new bone
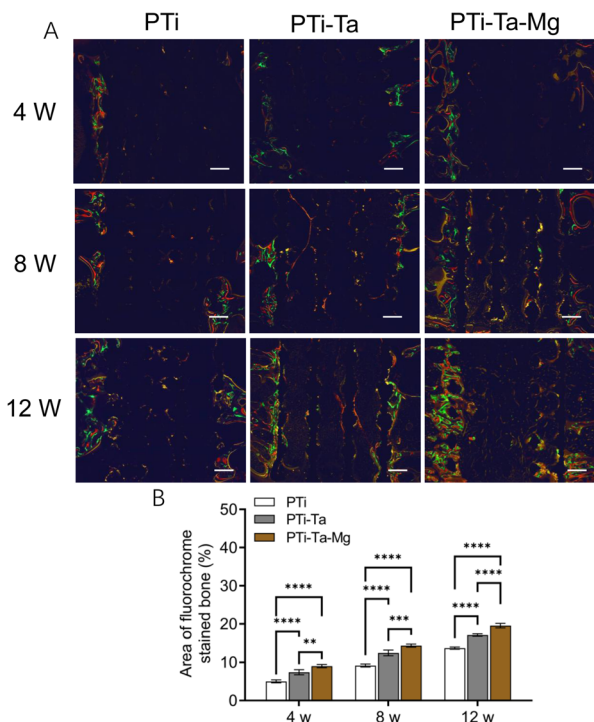

Fig. 4 X-ray radiographs of operated femoral condyle harvested at different times.

Fig. 6 (A) Fluorescent labeling images of new bone formation in different scaffolds implanted *in vivo* after 4, 8 and 12 weeks. Calcein: green staining; xylenol orange: red staining; tetracycline: yellow staining; scale bar = 1 mm; (B) quantitative analysis of these fluorescence densities. **: $p < 0.01$; ***: $p < 0.001$; ****: $p < 0.0001$.
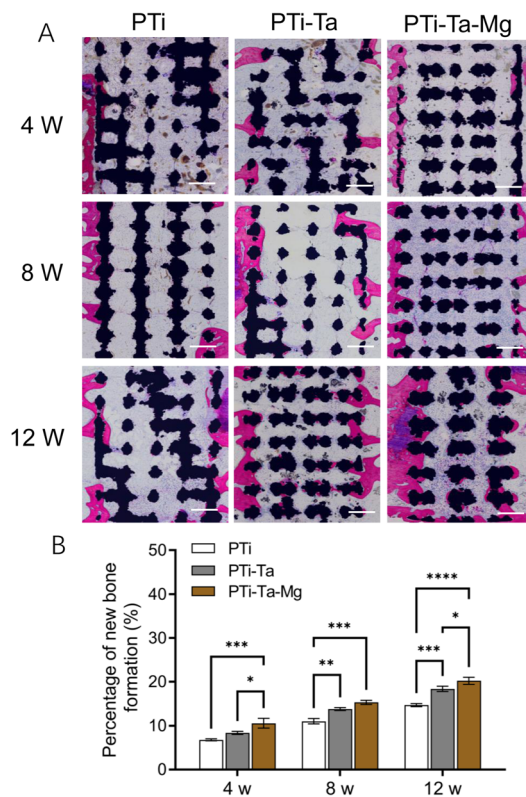

Fig. 7 (A) The histological staining of new bone formation in different scaffolds implanted *in vivo* after 4, 8 and 12 weeks. The red color represents the newly formed bone, the purple color represents the cartilage, and the black represents the scaffold. Scale bar = 1 mm. (B) Quantitative analysis of these newly formed bone. *: $p < 0.05$. **: $p < 0.01$; ***: $p < 0.001$; ****: $p < 0.0001$.

formed in the peripheral region but remained little in the central space. At week 12, in all groups, new bone in the peripheral region further increased. In particular, in PTi-Ta–Mg the new bone in the peripheral region became largely continuous and evidently denser compared with the other two groups. Additionally, small patches of new bone appeared in the central spaces of PTi-Ta and PTi-Ta–Mg. Image analyses found that, the percentage of new bone in PTi was 25% lower than in PTi-Ta ($p = 0.0006$) and 38% lower than PTi-Ta–Mg ($p < 0.0001$).

Discussion

In this study, the undoped and Mg-doped Ta_2O_5 coatings sequentially enhanced the *in vitro* osteoblastic activity of rBMSCs in 3D printed Ti6Al4V scaffolds and, more importantly, trabecular bone ingrowth into these scaffolds.

The sol–gel coatings fully covered the scaffolds, as was observed from the largely disappearance of loosely attached spherical Ti particles after coating deposition (Fig. 1B). The loosely attached particles originated from lack of melting by the laser beam; *in vivo* liberation of these particles is considered a risk associated with 3D printing of porous metallic implants.[23] To reduce their liberation and meet device approval regulations, these "unmelted" particles are removed by multiple techniques such as air stream blasting and chemical etching.[24,25] Interestingly, the effective encapsulation of these particles by the sol–gel coatings suggests that, it may also be a technique for

increasing the bonding between those particles to the scaffold, thus further reducing their liberation. In our previous study, we deposited coatings of <150 nm in thickness on planar substrates.[19] In the currently study, the coatings were likely micrometers in thickness locally, because the rough surface of the uncoated scaffold was able to retain more sol. The doping of Mg^{2+} into the Ta_2O_5 coating was straightforward and geometrical restrictions, compared with other coating techniques such as chemical vapor deposition and laser cladding.

The enhanced *in vitro* osteoblastic activity and *in vivo* bone ingrowth of PTi-Ta relative to PTi is generally consistent with our previous study[19] and several other studies.[11,26,27] In this study, the Ta ion release was relative low. This result was consistent with the report of Lu *et al.*[28] The low Ta ion release was related to its bioinert and high corrosion resistance. Thus, it was proposed that the positive effects of PTi-Ta on BMSCs was mainly attributed to the direct contact between the cells and scaffold surface. Ta coating deposition could increase the surface wettability and further enhance cell adhesion and proliferation, as well as differentiation.[19] In this study, on day 7, the ALP and Runx2 genes expressions were significantly higher in the PTi-Ta group compared with PTi group. On day 14, the OPN expression was significantly higher in PTi-Ta group compared with PTi. Since ALP is regarded as the early

osteogenic marker and OPN was the late osteogenic marker, it was confirmed that Ta coating could upregulate the expressions of osteogenic related genes at various stages. Similar positive results was also observed for BMSCs seeded into porous Ta scaffolds (vs. Ti6Al4V scaffolds).[29] Although the underlying mechanism was not fully understood, different mechanisms have been proposed to explain the improved (vs. titanium) stem cell response observed from Ta, such as the activation of the integrin α5β1/ERK1/2,[30] Wnt/β-catenin,[31] TGF-β/smad,[31] or MAPK/ERK[27] signaling pathway. Additionally, one study reported inhibition of osteoclastic activity by Ta.[31] It is possible that, some or all of these pathways are implicated in the increased osteoblastic activity and bony ingrowth observed in the present study, but this has not been investigated. Future studies are needed to systematically unravel all contributing signalling pathways.

The further enhancement of PTi-Ta–Mg relative to PTi-Ta is not fully understood, but may be explained based on clues from other studies. Díaz-Tocados et al.[32] observed that supplementing the Mg^{2+} concentration from 0.8 to 1.8 mM remarkably upregulated the expression levels of osteoblastic genes in bone mesenchymal stem cells and increased their in vitro mineralization. Furthermore, Mg^{2+} was found to elicit these effects via the Notch1 signaling pathway. In our study, the highest Mg^{2+} concentration released into PBS ($\sim$4.8 μg ml^{-1}) is markedly lower than the effective ranges reported by Díaz-Tocados et al.; thus, whether the cells were affected by that pathway is unknown. However, two ion implantation studies reported positive effects of comparably low Mg^{2+} concentrations on stem cells. Wang et al.[33] implanted Mg^{2+} into Ti with hierarchical surface topography for 30 or 60 min; after immersion in DMEM for 12 days, the samples released $\sim$0.5 and 1.0 μg cm^{-2} Mg^{2+}. However, the samples bearing these relatively low doses of Mg^{2+} substantially increased the proliferation and osteoblastic activity of rBMSCs. Kim et al.[34] implanted 2.3×10^{16} Mg^{2+}/cm^2 (i.e., $\sim$0.92 μg cm^{-2}) into Ti, and also observed significantly elevated proliferation and ALP activity of human BMSCs. Thus, the Mg ion release concentration in this study was involved in the effective dose. Collectively, the results of previous and the present studies suggest that, surface-loaded Mg^{2+} can stimulate the osteoblastic differentiation and osteogenic activity of BMSCs at low doses. Therefore, the sol–gel route reported here provides a straightforward method of modulating the Mg^{2+} fraction in Ta_2O_5 coating, and future studies will be performed to clarify this.

Conclusion

Undoped and Mg-doped sol–gel Ta_2O_5 coatings were homogeneously applied on 3D-printed Ti6Al4V scaffolds. Compared with uncoated scaffolds, those coated with undoped and Mg-doped Ta_2O_5 displayed sequentially elevated in vitro proliferation, osteoblastic gene expression, and mineralization of rBMSCs. After implantation in rabbit femoral condyles, bone ingrowth also followed this trend. These results indicate that, Mg-doped Ta_2O_5 coating is an effective technique for promoting the integration of Ti6Al4V scaffolds with trabecular bone.

Author contributions

Bo Zhang: conceptualization, methodology, investigation, writing–original draft. Jun Feng: conceptualization, methodology, investigation, writing–original draft. Shuo Chen: methodology, investigation. Chengdong Zhang: methodology, investigation. Xuwei Luo: validation, investigation; Zelong Yang: validation, investigation. Dongqin Xiao: conceptualization, methodology, investigation, writing-review & editing. Kui He: conceptualization, supervision. Ke Duan: conceptualization, methodology, funding acquisition.

Conflicts of interest

The authors declare that they have no known competing financial interests or personal relationships that could have appeared to influence the work reported in this paper.

Acknowledgements

References

1 Y. Bozkurt and E. Karayel, J. Mater. Res. Technol., 2021, 14, 1430–1450.

2 K. Dai, Z. Yang, L. Ding, Z. Yang, F. Hang, X. Cao, D. Chen, F. Zhao and X. Chen, Ceram. Int., 2023, 49, 19773–19785.

3 T. Hanawa, Sci. Technol. Adv. Mater., 2022, 23, 457–472.

4 H. Tschernitschek, L. Borchers and W. Geurtsen, J. Prosthet. Dent., 2006, 96, 12.

5 J. D. Bobyn, R. A. Poggie, J. J. Krygier, D. G. Lewallen, A. D. Hanssen, R. J. Lewis, A. S. Unger, T. J. O'Keefe, M. J. Christie, S. Nasser, J. E. Wood, S. D. Stulberg and M. Tanzer, J. Bone Jt. Surg., 2004, 86, 123–129.

6 G. Huang, S. Pan and J. Qiu, Materials, 2021, 14, 2647.

7 H. Gao, J. Yang, X. Jin, X. Qu, F. Zhang, D. Zhang, H. Chen, H. Wei, S. Zhang, W. Jia, B. Yue and X. Li, Mater. Des., 2021, 210, 110095.

8 F. Wang, C. Li, S. Zhang and H. Liu, Surf. Coat. Technol., 2020, 382, 125161.

9 R. Rambani, M. Nayak, M. S. Aziz and K. Almeida, Arch. Bone Jt. Surg., 2022, 10, 385–394.

10 M. Lu, P. Wu, X. Guo, L. Yin, H. Cao and D. Zou, Eur. Rev. Med. Pharmacol. Sci., 2018, 22, 7087–7104.

11 L. Wang, X. Hu, X. Ma, Z. Ma, Y. Zhang, Y. Lu, X. Li, W. Lei and Y. Feng, Colloids Surf., B, 2016, 148, 440–452.

12 K. B. Sagomonyants, M. Hakim-Zargar, A. Jhaveri, M. S. Aronow and G. Gronowicz, *J. Orthop. Res.*, 2011, **29**, 609–616.

13 V. K. Balla, S. Banerjee, S. Bose and A. Bandyopadhyay, *Acta Biomater.*, 2010, **6**, 2329–2334.

14 W. T. Lin, Z. W. Lin, T. Y. Kuo, C. S. Chien, J. W. Huang, Y. L. Chung, C. P. Chang, M. Z. Ibrahim and H. T. Lee, *Surf. Coat. Technol.*, 2022, **437**, 128356.

15 L. Ma, S. Cheng, X. Ji, Y. Zhou, Y. Zhang, Q. Li, C. Tan, F. Peng, Y. Zhang and W. Huang, *Mat. Sci. Eng. C*, 2020, **117**, 111303.

16 T. Qi, J. Weng, F. Yu, W. Zhang, G. Li, H. Qin, Z. Tan and H. Zeng, *Biol. Trace Elem. Res.*, 2021, **199**, 559–567.

17 L. Sun, X. Li, M. Xu, F. H. Yang, W. Wang and X. F. Niu, *Regener. Biomater.*, 2020, **7**, 391–401.

18 P. Gao, B. Fan, X. Yu, W. Liu, J. Wu, L. Shi, D. Yang, L. Tan, P. Wan, Y. Hao, S. Li, W. Hou, K. Yang, X. Li and Z. Guo, *Bioact. Mater.*, 2020, **5**, 680–693.

19 S. Chen, C. Zhang, D. Xiao, F. Shi, K. Liu, Y. Wan, K. Duan, J. Weng, G. Feng and Y. Yin, *Surf. Coat. Technol.*, 2021, **426**, 127769.

20 S. Wang, Z. Huang, L. Liu, Z. Shi, J. Liu, Z. Li and Y. Hao, *Mater. Des.*, 2021, **212**, 110242.

21 Q. Zhao, F. Yang, C. D. Zhang, S. Chen, X. Sun, B. Zhang, D. Q. Xiao, K. Liu, G. Feng and K. Duan, *Chin. J. Tissue Eng. Res.*, 2020, **24**, 2985.

22 J. Li, A. Ahmed, T. Degrande, J. De Baerdemaeker, A. Al-Rasheed, J. J. van den Beucken, J. A. Jansen, H. S. Alghamdi and X. F. Walboomers, *Dent. Mater.*, 2022, **38**, 613–621.

23 B. Wysocki, J. Idaszek, J. Buhagiar, K. Szlązak, T. Brynk, K. J. Kurzydłowski and W. Święszkowski, *Mater. Sci. Eng. C*, 2019, **95**, 428–439.

24 B. Wysocki, J. Idaszek, K. Szlązak, K. Strzelczyk, T. Brynk, K. J. Kurzydłowski and W. Święszkowski, *Materials*, 2016, **9**, 197.

25 S. Ferraris and S. Spriano, *Metals*, 2021, **11**, 1343.

26 F. Wang, L. Wang, Y. Feng, X. Yang, Z. Ma, L. Shi, X. Ma, J. Wang, T. Ma, Z. Yang, X. Wen, Y. Zhang and W. Lei, *Sci. Rep.*, 2018, **8**, 8927.

27 X. Dou, X. Wei, G. Liu, S. Wang, Y. Lv, J. Li, Z. Ma, G. Zheng, Y. Wang, M. Hu, W. Yu and D. Zhao, *J. Orthop. Translat.*, 2019, **19**, 81–93.

28 W. T. Lu, L. C. Zhang and J. Xu, *Corros. Sci.*, 2022, **196**, 110034.

29 Y. Guo, K. Xie, W. Jiang, L. Wang, G. Y. Li, S. Zhao, W. Wu and Y. Q. Hao, *ACS Biomater. Sci. Eng.*, 2018, **5**, 1123–1133.

30 M. Lu, X. Zhuang, K. Tang, P. Wu, X. Guo, L. Yin, H. Cao and D. Zou, *Cell. Physiol. Biochem.*, 2018, **51**, 589–609.

31 L. Shi, A. Wang, F. Zang, J. Wang, X. Pan and H. Chen, *Colloids Surf., B*, 2017, **160**, 22–32.

32 J. M. Díaz-Tocados, C. Herencia, J. M. Martínez-Moreno, A. Montes de Oca, M. E. Rodríguez-Ortiz, N. Vergara, A. Blanco, S. Steppan, Y. Almadén, M. Rodríguez and J. R. Muñoz-Castañeda, *Sci. Rep.*, 2017, **7**, 7839.

33 G. Wang, J. Li, W. Zhang, L. Xu, H. Pan, J. Wen, Q. Wu, W. She, T. Jiao, X. Liu and X. Jiang, *Int. J. Nanomed.*, 2014, **9**, 2387–2398.

34 B. Kim, J. Kim, Y. Park, B. Choi and J. Lee, *Mater. Sci. Eng. C*, 2013, **33**, 1554–1560.

© 2023 The Author(s). Published by the Royal Society of Chemistry